Ocean Engineering 186 (2019) 106108

Contents lists available at ScienceDirect

Ocean Engineering

journal homepage: www.elsevier.com/locate/oceaneng

A numerical and experimental investigation of the effect of side walls on hydrodynamic model testing in a wave flume

N. Xie [a,*], M. Hann [a], R. Pemberton [a], G. Iglesias [b], D. Greaves [a]

[a] School of Engineering, University of Plymouth, Plymouth, UK
[b] School of Engineering, University College Cork, Cork, Ireland

ARTICLE INFO

Keywords:
Side wall effect
3D rankine method
Numerical prediction
Model test
Artificial damping

ABSTRACT

The side wall effect was normally tackled by potential flow based numerical methods. It is well known that, due to the existence of the resonance frequency in the wave tank, the numerical methods over-predict the hydrodynamic forces when comparing with model experiments. Furthermore, in most of the previous studies on the effects of the side walls, the model was located at the centre of the tank, the disturbances on both sides of the model are symmetric, and the resonances of some of the responses such as wave surface elevation and motions may not be excited at the tank natural frequencies. In the present study, a Rankine source panel method is used to tackle the effects of the side walls and artificial damping is introduced in the free surface boundary condition to account for the viscous damping effect. Model experiments are carried out for a lifeboat model located at various positions in a wave flume. Numerical results of the wave forces, free surface elevations and motions of the model are compared with the model test measurements, and good agreement is found. It is shown that the inclusion of the artificial damping in the free surface boundary condition is effective, in particular for the model at off-centre position of the tank.

1. Introduction

The wave model testing facilities (wave basin, towing tank and wave flume) always have a limited width. Due to the existence of the side walls, the measured loads and responses would present some discrepancies compared to the open sea results (e.g., Kashiwagi and Ohkusu, 1989). ITTC has a recommended procedure for seakeeping model experiments to avoid the tank wall interference in head waves in towing tank (ITTC, 2002). The recommended maximum frequency at which tank wall interference occurs depends on Froude number of the model, which means for model tests at low and zero speeds, the side wall interference is inevitable, therefore, there will be a strong interest to assess the side wall effects when extrapolating the experimental results to open sea condition in full scale. The side wall effects also present for a floating structure in a channel, in this case, the floating structure may located on off-central position of the channel to avoid the passing vehicles. Another situation where the wall effect is relevant is for a launch and recovery operation at sea, when a lifeboat or ROV is in between two large vessels (mothership and rescue/support vessel), where the mothership/rescue vessels are considerably large than the lifeboat/ROV, and when considering the hydrodynamic interactions, they are replaced as infinitely long walls.

The side wall effect was tackled numerically by means of the free surface Green function method based on potential flow theory. The free surface Green function in the open sea satisfies the Laplace equation, linearized free surface condition, sea bottom condition and radiation condition at the far field, but not the boundary condition on the two parallel side walls. One way to tackle the problem is to consider the side wall as an independent, fixed (very large) body, so that the singularity is distributed on the wetted body surface, cf. Duan et al. (2007) and Peng et al. (2015).

McIver (1993) presented a theoretical model for diffraction and radiation solutions on truncated vertical cylinders including side wall effects through the multipoles expansion method. This method is limited to bodies of simple geometry such as vertical cylinders. For general 3d problem, a Green function satisfying the boundary condition on the side walls should be defined. Linton (1993) proposed a free surface Green functions with tank walls. Kashiwagi (1991) divided the Green function involved in the side wall effects into an open sea Green function and another term, and the slowly convergent term was replaced by a double integral over a semi-infinite domain. Chen (1994) presented the tank Green function as the sum of two parts based on the convergence. Due to

* Corresponding author.
E-mail address: nan.xie@plymouth.ac.uk (N. Xie).

https://doi.org/10.1016/j.oceaneng.2019.06.013
Received 9 January 2019; Received in revised form 29 May 2019; Accepted 2 June 2019
Available online 13 June 2019

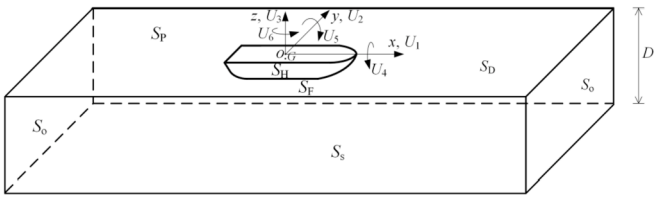

Fig. 1. Definition of the coordinate system, motions and domain boundary.

the slow convergence of the Green function, Xia (2001) divided it into three parts in the near, middle and far fields, respectively. Newman (2016) developed the Image Green Function (IGF) method, which is composed of a series of open-sea Green functions satisfying the free surface condition. Chen et al. (2018) investigated hydrodynamics of side wall effects through the IGF based on Taylor expansion boundary element method.

The Rankine source panel method is an alternative approach for tackling the wave-body interaction problem. The Rankine source is easy to calculate numerically, but it does not satisfy the linearized free surface boundary condition and the radiation condition in the far field. Early efforts can be seen from works of Yeung (1982) for 2D and Liapis and Beck (1985) for 3D problems. For the wave-body interaction problem in open sea, the Rankine singularity needs to be distributed on both the hull surface and the free surface, and the radiation condition should be implemented properly in the frequency domain (Nakos, 1989, Cao et al., 1989, Bertram and Thiart, 1998; Bunnik, 1999, Xie and Vassalos, 2012) or in time domain (Watai et al., 2015, 2016). It can also be applied for hydrodynamics analysis of a hydrofoil under free surface (Xie and Vassalos, 2007). The Rankine panel method has the flexibility of altering the free surface boundary condition to tackle higher order or nonlinear problems (Boo, 2002; Ning et al., 2018). More recently, resonance of wave surface motion in the gap between a FPSO and an LNG tanker has attracted much interest in the hydrodynamics research community (Soares et al. (2015); Sun et al. (2015); Pessoa et al. (2015); Zhao et al. (2018)). The potential flow based panel method was used for the numerical prediction. Model experimental results had to be used to tune the artificial damping coefficients in the free surface boundary condition to achieve good agreements.

Yuan et al. (2018) investigated side wall effects on ship model testing in a towing tank in calm water and in waves using the Rankine source panel method. It was found that the side wall effect on the experiments in waves is more complicated than that in calm water due to the complexity of the wave systems. The hydrodynamic coefficients (radiation forces) fluctuated wildly away from the open sea results. The reflected and radiated waves were trapped within the towing tank and resulting side wall effects become significant.

In most of the research into the side wall effect, the model was positioned at the centre of the tank. In the present study, side wall effects are investigated both numerically and experimentally, and the model was located at various distances from the side wall. In the numerical study, the Rankine source panel method was used to solve wave field. The singularities were distributed on the hull surface, free surface side walls and far field control surface, and an artificial damping term was added to the free surface boundary condition. Model experiments were carried out in a wave flume for a lifeboat model. Wave loading on the hull, free surface elevations and model motions were predicted and compared with those of the model experiments. Comparison of the numerical prediction and the model experiments shows good agreement. It was found that adding the artificial damping in the free surface boundary condition leads to better agreement between the numerical results and the measurements, in particular for the model at off-central positions of the flume.

2. Numerical methods

It is assumed that the fluid is inviscid and incompressible, and that the motion is irrotational, velocity potentials exist and satisfy the Laplace equation in the fluid domain. The right-handed Cartesian coordinate system is defined with *xoy*-plane on the undisturbed free surface, while *xoz*-plane is the symmetric vertical plane of the ship model; *ox*-axis pointing to the bow and *oz* is positive upwards and through the centre of gravity, CG, of the model (Fig. 1).

A complex velocity potential provides a description of the velocity potential as

$$\Phi(x,y,z,t) = Re\left\{\left[\varphi_0(x,y,z) + \varphi_7(x,y,z) + \sum_{j=1}^{6} U_j\varphi_j(x,y,z)\right]e^{-i\omega t}\right\} \tag{1}$$

where φ_0 and φ_7 are complex spatial velocity potentials for the incident and diffraction waves, respectively; $U_j, j = 1, 2, \ldots, 6$, are the complex velocity amplitudes of motions of the 6 degree of freedom for the body (U_1,surge; U_2, sway; U_3,heave; U_4, roll; U_5, pitch; U_6, yaw); $\varphi_j, j = 1, 2, \ldots, 6$, are the spatial radiation potentials.

The boundary value problems for the velocity potentials are described in Appendix A. The boundaries of the fluid domain consist of the wetted hull surface, S_H; free surface, S_F; damping zone free surface, S_D; port side wall, S_P; starboard side wall, S_S; the far field control surface at both ends of the flume, S_O and the bottom, S_B.

The Green function is selected as

$$G(x,y,z;\xi,\eta,\zeta) = \frac{1}{\sqrt{(x-\xi)^2+(y-\eta)^2+(z-\zeta)^2}} + \frac{1}{\sqrt{(x-\xi)^2+(y-\eta)^2+(z+2D+\zeta)^2}} \tag{2}$$

where (x, y, z) is the field point; (ξ, η, ζ) is the source point and D is the water depth. Since the Green function in (2) satisfies the bottom boundary condition (A-16), source distribution on the bottom boundary will not be required.

$$\varphi_j(x,y,z) = \iint_S G(x,y,z;\xi,\eta,\zeta)\cdot\sigma_j(\xi,\eta,\zeta)ds \tag{3}$$

where $\sigma_j, j = 1, 2, \ldots, 7$, are the source densities on the boundary surfaces and $S = S_H + S_F + S_D + S_P + S_S + S_O$, see Fig. 1. In order to surpass the irregular frequency, the water plane of the model is also panelised and zero normal velocity was applied (Malenica and Chen, 1998).

The free surface boundary condition with artificial damping is (see appendix A):

$$g\frac{\partial\varphi_j}{\partial z} - \left[\omega^2(1-\nu^2) - i\cdot 2\nu\omega^2\right]\varphi_j = 0 \quad \text{on } z = 0 \tag{4}$$

$j = 1, 2, \ldots, 7$, where ν is the non-dimensional artificial damping coefficient. The modified free surface condition also used by Chen (2004) and Faltinsen and Timokha (2015). In the recent works of Guo et al. (2018a, 2018b), a 2D time-domain Green function was developed and implemented numerically to account for the viscous effects in the free surface boundary condition in body-wave interaction problems. In their method, viscous damping is taken into account in the dynamic free surface boundary condition in the same manner as in the current study (equation (A-20)); however, the addition of the viscous damping in the kinematic free surface boundary condition is slightly different in that the wave surface elevation was eliminated before the addition of the viscous damping in the works of Guo et al.. In the present method, the overall free surface condition has an additional ν^2term. Since ν is usually a small number, the effect of the difference in the modified free surface boundary condition between the present method and that of Guo et al.'s on the hydrodynamic loads and motions is likely to be insignificant. The free surface boundary condition with viscous effect can also be derived

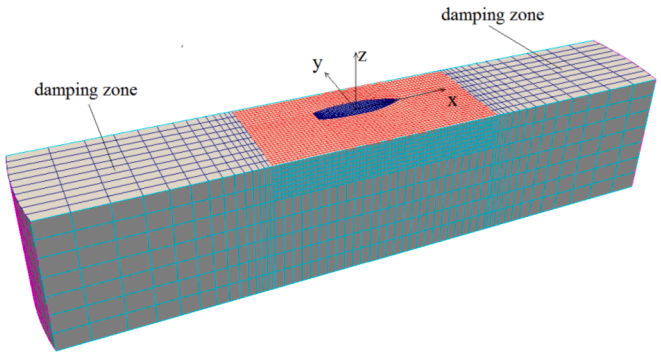

Fig. 2. The coordinate system and domain boundaries.

from linearization of NS equation (Chen and Dias, 2010). When $\nu = 0$, eq. (4) becomes the undamped linearized free surface boundary condition:

$$g\frac{\partial \varphi_j}{\partial z} - \omega^2 \varphi_j = 0 \quad \text{on} \quad z = 0 \tag{5}$$

The radiation condition is satisfied by applying an approximated Sommerfeld radiation condition (A-18) at the outer boundary, S_O, this was enhanced by setting up the damping zone on the free surface further away from the vessel model where size of the panel increases gradually (see Fig. 2) and an artificial damping coefficient was applied for the free surface boundary condition in the damping zone.

Equation (3) indicates that the velocity potentials at a field point (x, y, z) in the fluid domain (including at the domain boundary) can be represented by a source distribution over the domain boundary surfaces. In order to solve the unknown source strength in equation (3), the domain boundaries are discretized into a number of quadrilateral panels with constant source density. By applying the boundary conditions at the control point of each panel for every boundary of the fluid domain, one equation for the unknown source density will be obtained for each panel and the equations for the unknown source strength are closed and can be solved by a standard routine.

Once the unknown source distributions (and the velocity potentials) are solved, the complex amplitude of the spatial pressure distribution can be calculated as:

$$p_j(x, y, z) = i\rho\omega\varphi_j(x, y, z) \quad j = 0, 1, \ldots, 7 \tag{6}$$

The complex amplitudes of wave exciting forces/moments are

$$F_k = i\rho\omega \iint_{S_H} (\varphi_0 + \varphi_7) n_k ds \quad k = 1, 2, \ldots, 6 \tag{7}$$

The added mass and damping coefficients can be calculated as (see Appendix A)

$$A_{kj} = Re\left\{\rho \iint_{S_H} \varphi_j n_k ds\right\} \tag{8}$$

$$B_{kj} = \omega \cdot Im\left\{\rho \iint_{S_H} \varphi_j n_k ds\right\} \tag{9}$$

k, j=1,2, …,6. The equations of motions of the vessel model are

$$\sum_{k=1}^{6}\left\{-\omega^2(M_{kj} + A_{kj}) + i\omega B_{kj} + C_{kj} + C_{kj}^{'}\right\}X_k = F_j \tag{10}$$

where $j = 1, 2, \ldots, 6$, are for surge, sway, heave, roll, pitch and yaw motions, respectively. C_{kj} and $C_{kj}^{'}$, $k, j, = 1, 2, \ldots, 6$, are the restoring coefficients due to hydrostatics and the spring, respectively. Solutions of (10) are the amplitudes of vessel motions, $X_k, k = 1, 2, \ldots, 6$.

The complex amplitude of the spatial wave surface elevation for the diffraction problem is

Table 1
Main particulars of the test model.

Specifications	values
Length, L (m)	0.50
Beam, B (m)	0.149
Draft, T (m)	0.054
Displacement, Δ (kg)	1.36
CG above keel, $\overline{KG}$ (m)	0.054
Roll radius of gyration, k_{xx}/B	0.35
Pitch radius of gyration, k_{yy}/L	0.25
Yaw radius of gyration, k_{zz}/L	0.25

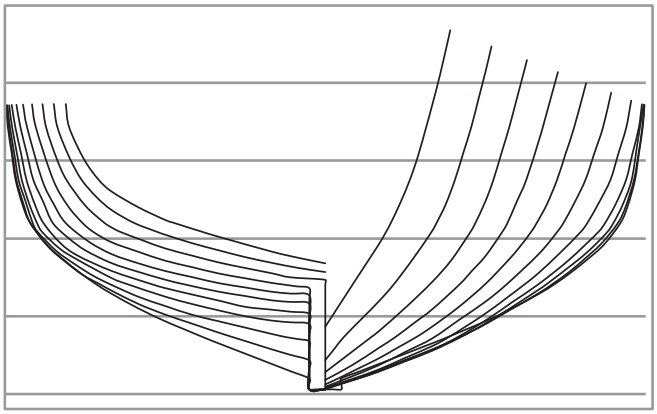

Fig. 3. Body-plan of the lifeboat.

Table 2
Specifications of the load cell.

Specifications	values
Nonlinearity - % FS	±0.1
Hysteresis - % FS	±0.1
Nonrepeatability – multi-axis loading	±0.10
Safe Overload -%RO	150
Operating temperature range (C)	−10 to 85
Rated Output-mV/V (Nominal)	±0.4
Maximum excitation Voltage	5V
Crosstalk	±0.1%
Protection	IP67
Diameter	6.0 cm
Height	4.0 cm
Weight	250g

$$\eta(x, y) = \frac{\omega}{g}[i\cdot\varphi_0(x, y, 0) + i\cdot\varphi_7(x, y, 0) - \nu\varphi_7(x, y, 0)] \tag{11}$$

3. Model experiments

The model experiments were conducted in a flume of 35 m long and 0.6 m width of the COAST Laboratory of the University of Plymouth. The flume was equipped with a piston type wave-maker with active absorption capabilities and a foam beach at the opposite end. Tests were carried out at still water depth of 0.75 m. A lifeboat model was manufactured from carbon composite, main particulars of the lifeboat model are shown in Table 1. The body plan of the lifeboat is shown in Fig. 3. Before the tests, the model was calibrated for its centre of gravity (CoG) and radius of gyration in each component direction (gyradii). The experiments consist of model fixed and free floating tests. For the fixed experiments, a 6-axis load cell was used to measure the wave load components acting on the model. The capacities of the load cell are 125 N for F_x and F_y, and 250 N for F_z; capacity of M_x, M_y and M_z are all 25 N.m. Accuracy of the load cell is ±0.1%. More specifications about

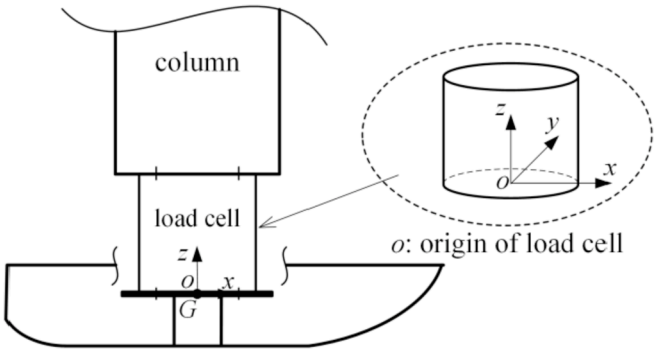

Fig. 4. Installation of the load cell with the lifeboat model.

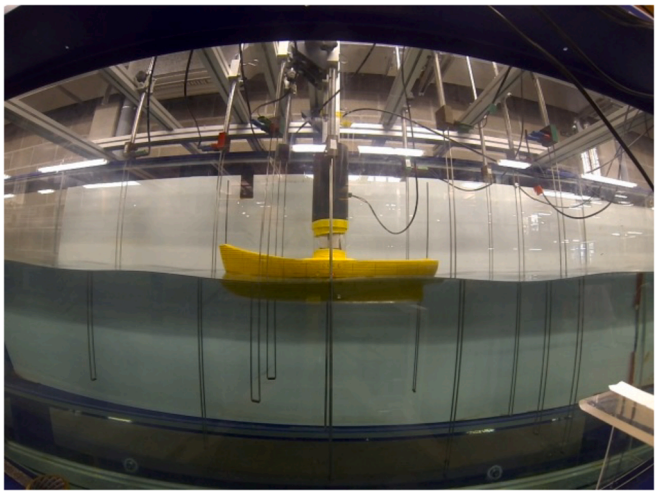

Fig. 5. The fixed model experiment.

the load cell are listed in Table 2. The model was fixed in place using a vertical column connected via the load cell at the model CoG position, see Fig. 4. The load cell is water proof (IP67), and is placed on a platform at the level of CoG of the model. To reduce the uncertainty of the measurement, due attention should be taken to ensure accurate alignments between the axes of the model and the load cell as well as the model with the wave flume. Wave probes were installed at various locations to register free surface elevations during the experiments, see Figs. 5 and 6. The separation gap, s, is defined as the distance between the starboard of the model and the flume wall, see Fig. 6. Locations of wave gauges P3, P4, P5 and P7 were also shown in the figure.

For the free floating experiments, the lifeboat model can move freely in waves but with two springs and wires attached at bow and stern of the model horizontally through pulleys, see Fig. 7. The connecting wires and the springs are in the longitudinal central plane of the model. The rate of the spring is 2.06 N/m. The 6DOF motions of the model were measured by an optical tracking system (Qualisys motion measurement system).

4. Results and discussions

Sensitivity and convergence analysis have been carried out for the numerical calculation considering domain size, boundary surface discretization scheme and the artificial damping coefficient in the damping zone free surface. For the results presented in the following sections, the longitudinal range of the free surface boundary, S_F, is one wave length ahead of the bow and one wave length after the stern of the model. The range of the damping zone free surfaces at both ends of the flume is five times the wave length. In the numerical calculations, 5772 panels are distributed on the domain boundaries (1475 panels on the body surface, 896 panels on each of the side walls, 1862 panels on the free surface, 340 panels on the damping zone, 112 panels on the outer surface and 191 panels on the water plane), see Fig. 2. The length of the panels on the lifeboat model is about $1/40^{th}$ of the boat length; there are 34 panels in the girth direction. On the free surface, S_F, for panels between the bow and stern of the model, length of the panel is 1/16th of model length; for the panels in front of the bow of the model or behind the stern of the model, the panel length is 1/20th of wave length, the maximum width of a free surface panel is 1/24th of the flume width (2.5 cm). The lengths of panels on the damping zone expand with a ratio of 1.20. The computational time for each frequency is about 45 min on a desktop using Intel® Core™ i7-2600 CPU @3.40 GHz and 64-bit Operating system.

Model experiments were conducted in regular waves. In analysing the data recorded during the experiments, time series of the raw data were selected after initial transient values had passed. The sampling frequency for the wave loads is 1613 Hz and for waves and motions of the lifeboat model, the sampling frequencies are 128 Hz. Any static offset was removed to yield oscillating responses only. Band-pass filtering was applied to the recorded signals to obtain first order responses (loads and motions).

4.1. Wave loads

All the wave loads were measured for the fixed lifeboat model cases. The model was held at 3 different distances from the side wall given the

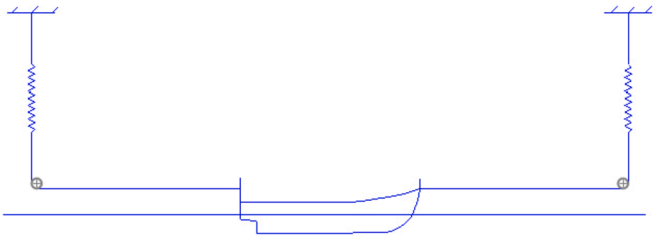

Fig. 7. The free floating experiments for the lifeboat model.

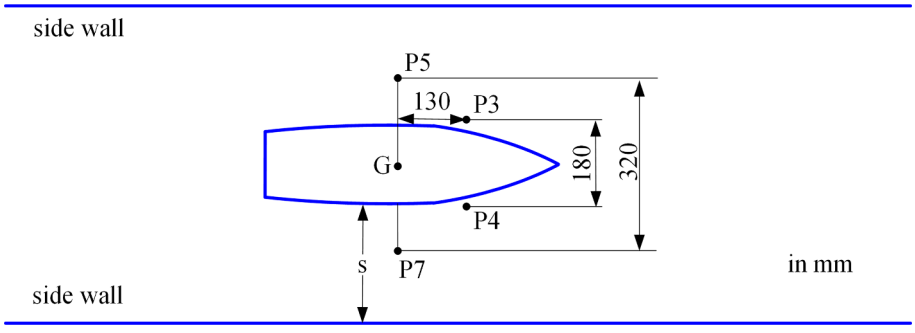

Fig. 6. The separation gap between the model and flume walls and wave gauge locations.

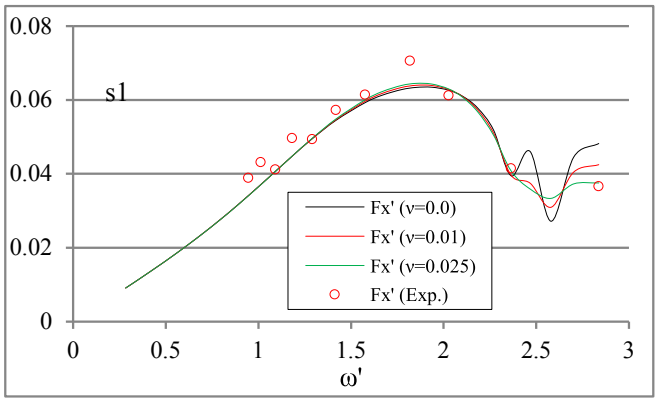

Fig. 8. Surge wave force for separation gap *s=s1*.

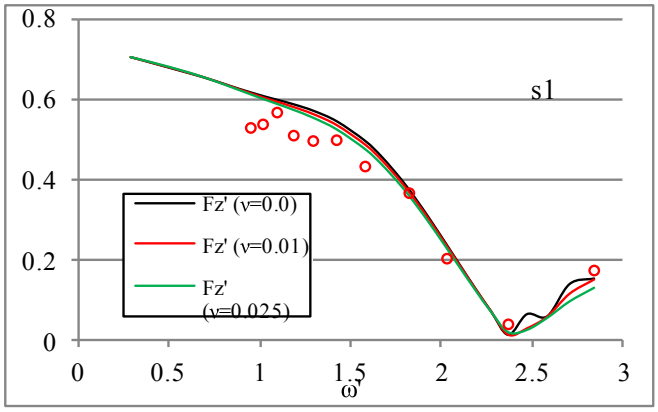

Fig. 9. Heave wave force for separation gap *s=s1*.

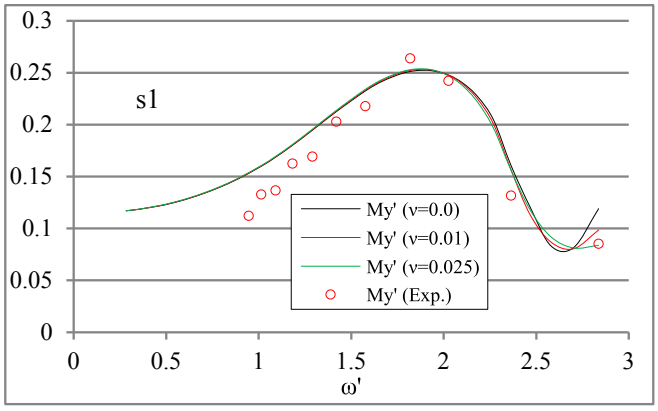

Fig. 10. Pitch moment for separation gap *s=s1*.

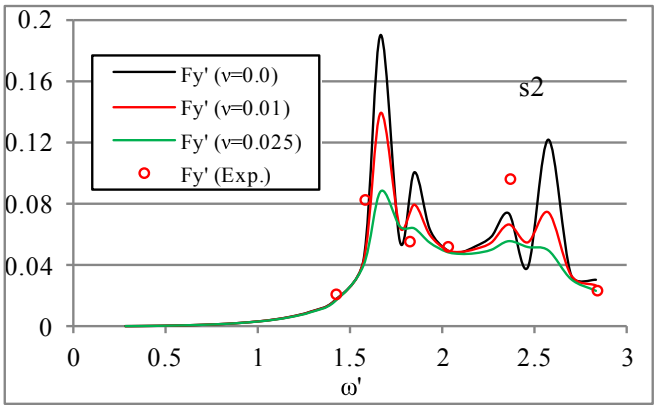

Fig. 11. Sway force for separation gap *s=s2*.

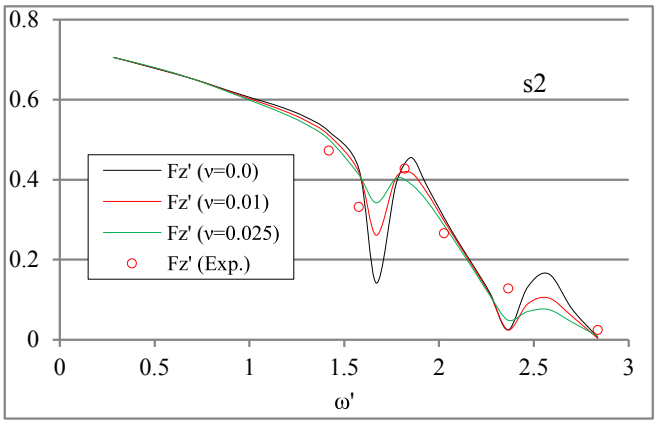

Fig. 12. Heave force for separation gap *s=s2*.

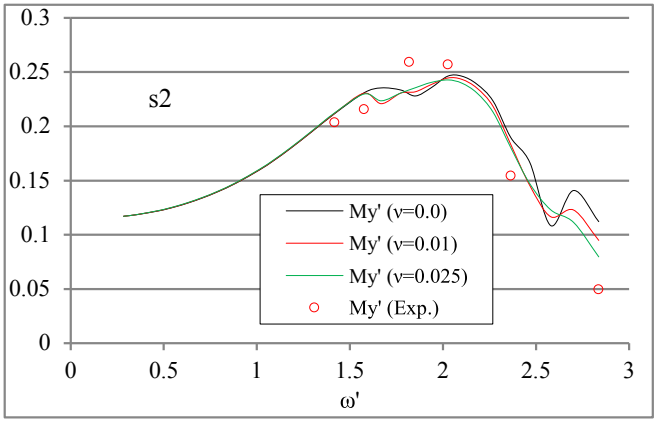

Fig. 13. Pitch moment force for separation gap *s=s2*.

separation gap $s1 = 22.5$ cm, $s2 = 15$ cm and $s3 = 7.5$ cm, where $s1 = 22.5$ cm represents the model at the central position of the flume. The experiments were carried out in linear regular waves. The force and moment amplitudes were non-dimensionalised by $\rho gLBa$ and ρgLB^2a, respectively, where ρ is the water density, g is the acceleration due to gravity, L and B are the length and beam of the lifeboat model, respectively, and a is the amplitude of the incident waves. The wave frequency was non-dimensionalised with $\omega' = \omega\sqrt{L/g}$.

Fig. 8–10 show the wave loads on the model for the separation gap *s=s1*, where the model is positioned at the centre of the flume. The agreement between the numerical and experimental results is satisfactory. It is noticed that the wave loads are not sensitive to the artificial damping coefficient, ν. There is very little difference among the wave loads for the three artificial damping coefficients: $\nu = 0.00, 0.01$, and 0.025, except at the higher frequency region, where $\nu = 0.025$ has a better agreement with the experiment.

Fig. 11–13 are the sway, heave forces and pitch moment for the separation gap *s=s2*. The predicted heave force and pitch moment are in good agreement with the measurement. For the sway force, the largest peak for the numerical prediction is at a frequency corresponding to the first resonance mode of the flume width (wave length $\lambda = 1.2$ m), which is over-predicted by the numerical method. The measured data shows a peak at the second resonance mode (wave length $\lambda = 0.6$ m), but the

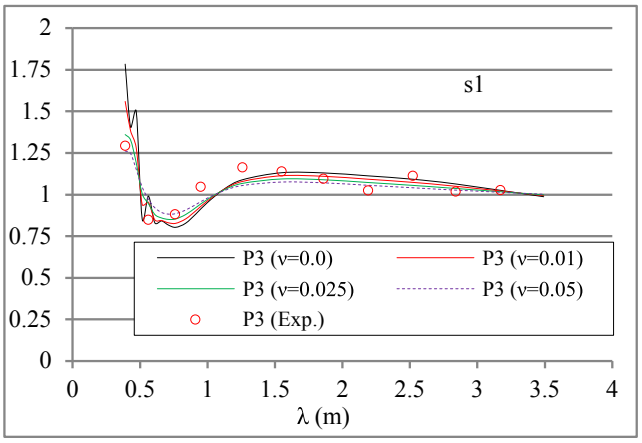

a)

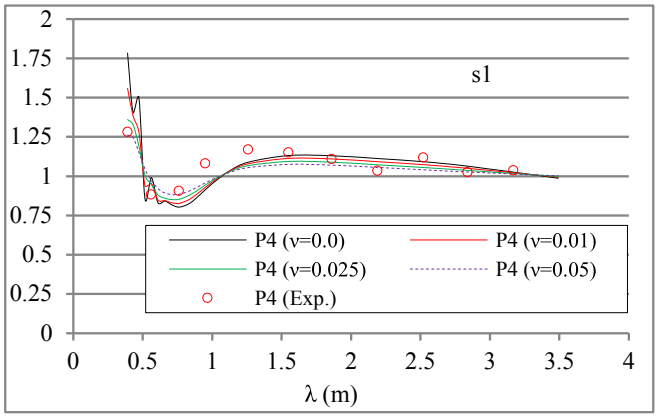

b)

Fig. 14. Free surface elevations for separation gap *s=s1* (a) for P3 and (b) for P4.

peak in the numerical prediction is much smaller. The second largest peak of the numerical prediction is at a wave length close to the third flume width resonance frequency ($\lambda = 0.4$ m). Overall, except for the second flume width resonance frequency ($\lambda = 0.6$ m), the numerical results with the free surface artificial damping coefficient $\nu = 0.025$ show good agreement with the model experimental measurements.

4.2. Free surface elevation

The free surface elevations for the fixed model tests at the selected positions were calculated by the numerical method and compared with the model experiment measurements. The wave amplitudes are non-dimensionalised by the amplitude of the incident wave. Fig. 14 shows the comparison of wave amplitudes at wave gauge locations P3 and P5 against wave length, λ, for the separation gap *s=s1* (model at the centre of the flume). Results of four artificial free surface damping coefficients ($\nu = 0$, 0.01, 0.025, 0.05) for the numerical results are shown. The agreement between the numerical and model experimental results is satisfactory. It can be seen that the effect of the damping coefficient on the numerical results is minor. Wave amplitudes with the undamped free surface boundary condition show small spikes at the second and third flume width resonance frequencies ($\lambda = 0.6$ m, 0.4 m).

Fig. 15 shows comparison of waves at P5 and P7 for the gap separation *s=s2* (model at off-central position). At the short wave length range, the numerical results with undamped free surface condition

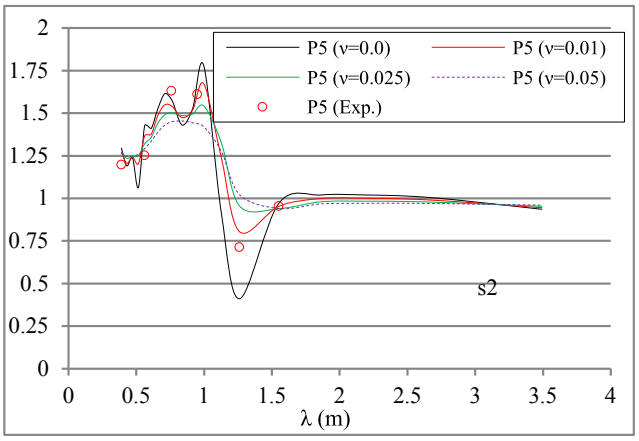

a)

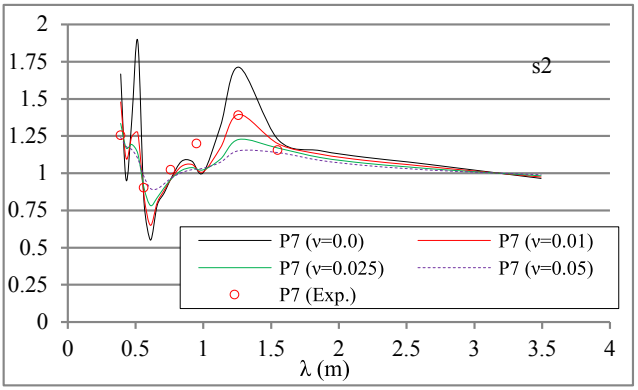

b)

Fig. 15. Free surface elevations for *s=s2* (a) for P5 and (b) for P7.

change sharply at the first three flume width resonance frequencies due to the interaction and lack of damping in the numerical model. The numerical results with the artificial damping for the free surface boundary condition are smooth and agree well with the experimental results. Fig. 17 is a snapshot of the diffraction wave field (incident and diffraction waves) for the separation gap *s=s2*. It is interesting to note the substantial differences between the wave elevations at the port and starboard sides of model when the wave length is close to the first and second resonance modes of the flume width (λ=1.2 m, 0.6 m).

In Fig. 16, the wave elevations at P3 and P4 for the gap separation *s=s3* is plotted. The numerical results show more peaks, indicating more resonances at the high frequency (short length) wave range. It seems that setting the artificial damping coefficient equal 0.01 leads to better agreement between the measured and numerical results. The wave elevations at the starboard side (P3, closer to the wall) are much larger than the port side (P4) due to the side wall effect. There is a peak at wave length $\lambda = 0.43$ m in the numerical prediction which is close to the third resonance frequency of the flume width.

4.3. Model motions

Some of the hydrodynamic coefficients of radiation (added mass and

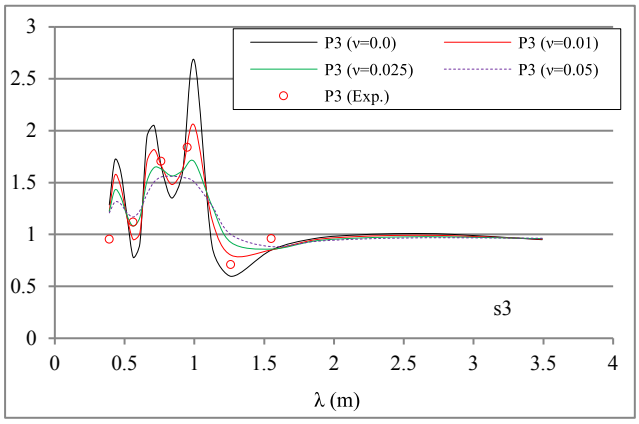

a)

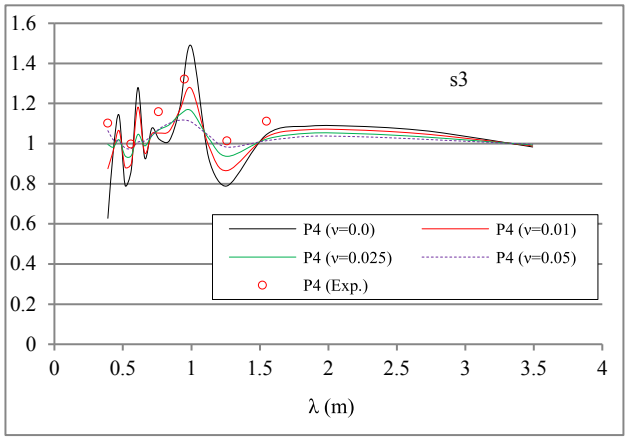

b)

Fig. 16. Free surface elevations for *s=s3* (a) for P3 and (b) for P4.

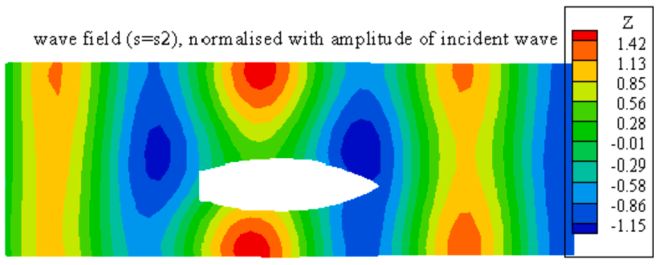

Fig. 17. Snapshot of the diffraction wave field for separation gap *s=s2*.

damping coefficient) were selected and shown in Fig. 18–21. The non-dimensional added masses are defined as: $A_{33}^{'} = A_{33}/m$, $A_{22}^{'} = A_{22}/m$, where m is the mass of the model and the non-dimensional damping coefficient is defined as: $B_{55}^{'} = B_{55}/mL\sqrt{gL}$. Fig. 18 is the heave added mass at the separation gap *s=s1*, with the model in the centre of the flume. A peak at the second flume width resonance frequency ($\lambda = 0.6$ m) is clearly seen. As the artificial damping increases, the added mass is smooth. Fig. 19 shows the sway added mass for *s=s2*, in which the model is at an off-centre position. The peaks at the first and second resonances were observed. The magnitudes at the peaks decrease as the artificial damping increases as expected. Fig. 20 is the heave added mass for the separation gap *s=s2,* substantial difference from the heave added

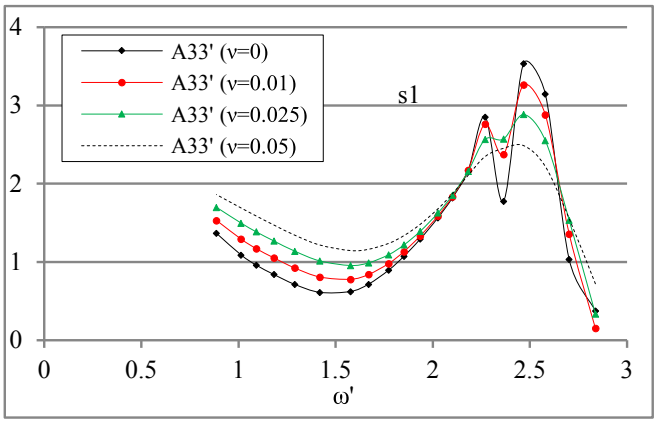

Fig. 18. Heave added mass for separation gap *s=s1*.

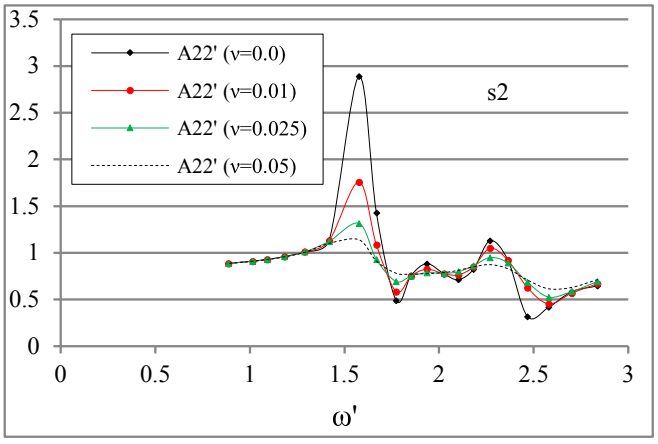

Fig. 19. Sway added mass for separation gap *s=s2*.

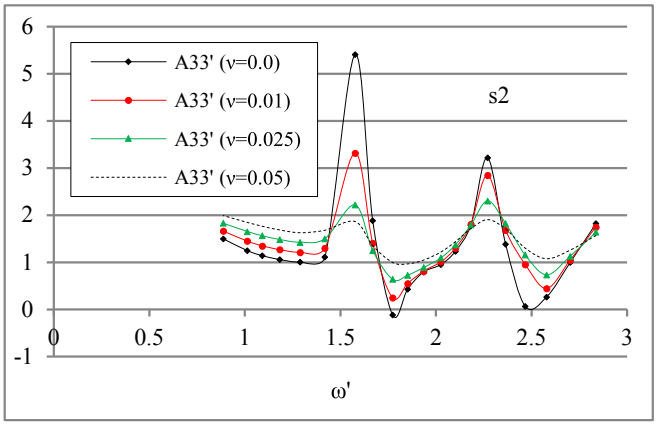

Fig. 20. Heave added mass for separation gap *s=s2*.

mass with *s=s1* (Fig. 18) can be seen due to the wall effect. A large peak at the third resonance ($\lambda = 0.4$ m) can be observed from the pitch damping coefficient in Fig. 21.

The motion RAOs of the model for separation gap *s=s1* (model at centre of the flume) are shown in Fig. 22–24. The amplitudes of surge, sway and heave are non-dimensionalised with the amplitude of the incident wave (a), pitch amplitude was non-dimensionalised with the amplitude of slope of the incident wave ($k_0 a$), where k_0 is the wave number. It can be seen that the agreement between the numerical prediction and model experiment are generally good. For the numerical

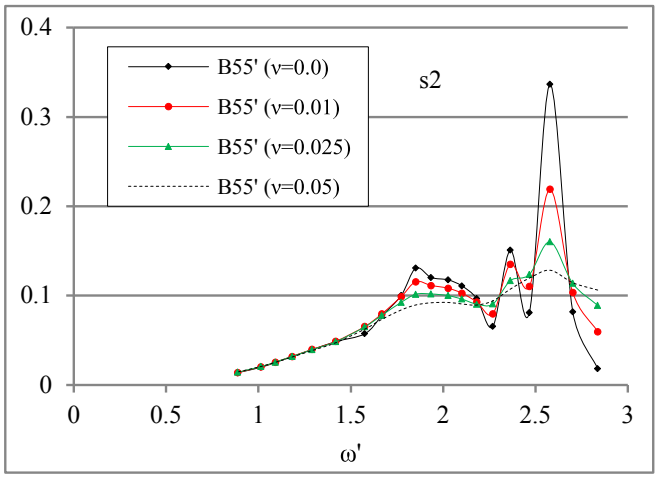

Fig. 21. Pitch damping coefficient for separation gap *s=s2*.

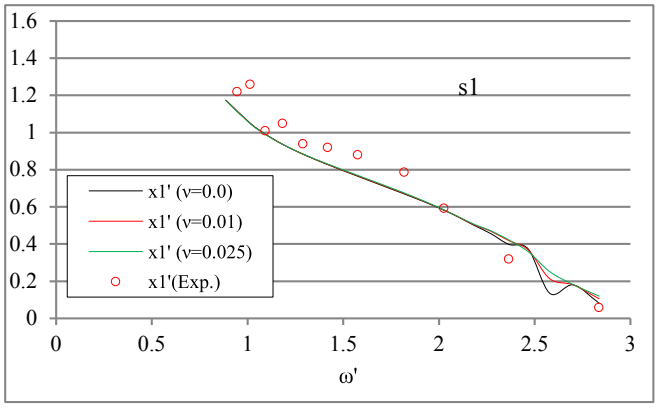

Fig. 22. Surge RAO for separation gap *s=s1*.

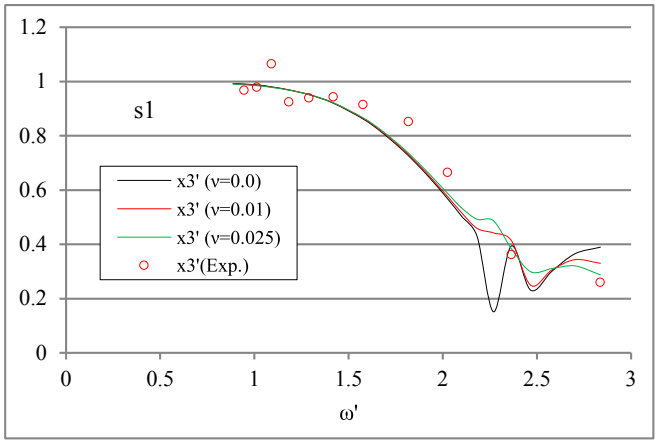

Fig. 23. Heave RAO for separation gap *s=s1*.

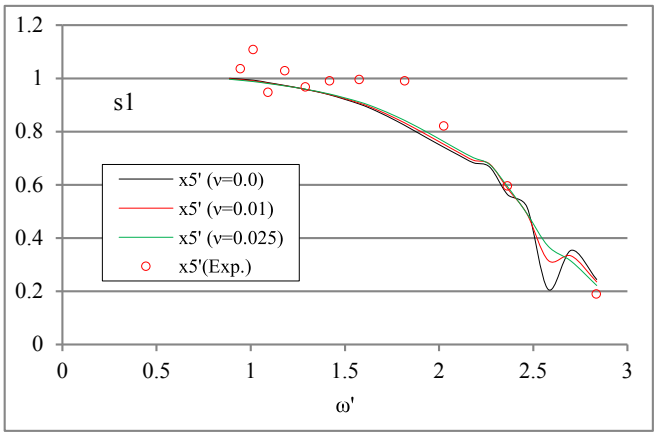

Fig. 24. Pitch RAO for separation gap *s=s1*.

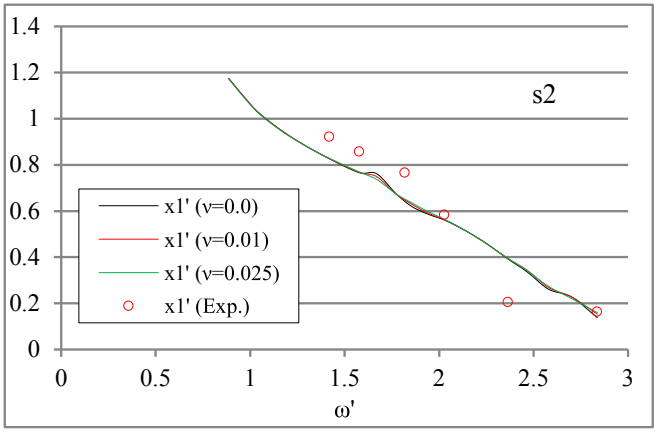

Fig. 25. Surge RAO for separation gap *s=s2*.

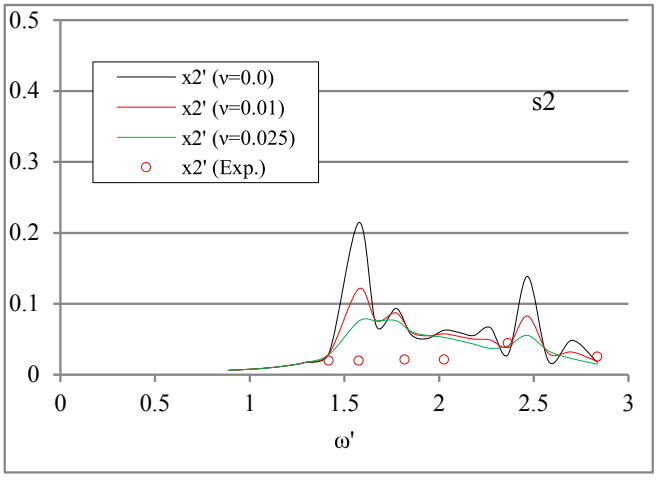

Fig. 26. Sway RAO for separation gap *s=s2*.

prediction with undamped free surface boundary condition, there are troughs in the high frequency range due to the resonance; the troughs disappear when the artificial damping applied in the free surface condition.

For separation gap *s=s2*, the comparisons are shown in Fig. 25–28. The model is on off-central position of the flume in this case. The effect of the walls on the model is stronger, as can be seen from heave motion in Fig. 27, where resonance at the first mode of the flume width occurs even when a higher artificial damping coefficient was applied in the free surface boundary condition than for the *s=s1* case (Fig. 23). The sway motion is over-predicted by the numerical model due to non-consideration of viscosity in the potential flow theory. Overall, the agreement between the numerical and experimental results is reasonably satisfactory when the artificial damping was introduced.

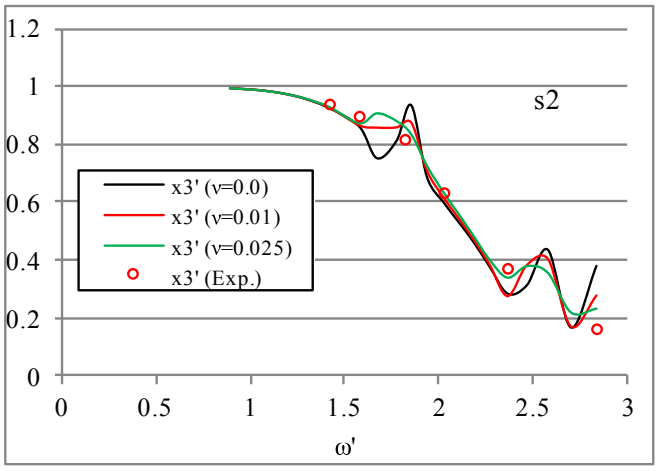

Fig. 27. Heave RAO for separation gap *s=s2*.

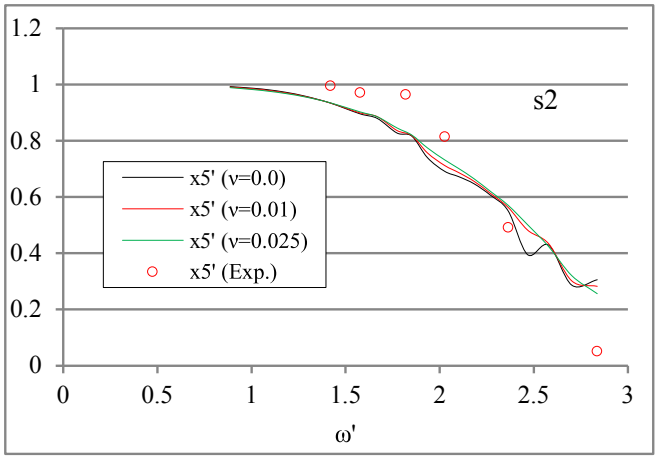

Fig. 28. Pitch RAO for separation gap *s=s2*.

5. Conclusions

The side wall effect was traditionally tackled with potential flow based methods. It is well known that, due to the existence of the resonance frequencies in the wave tank, the numerical methods over-predict the hydrodynamic forces. Furthermore, in most of the previous studies on the effect of the side wall, the model was located at the centre of the wave tanks, due to the symmetry of the disturbance on both sides of the model, resonances of some of the responses, such as wave surface elevations, motions of the model in waves may not be excited at the natural frequencies. However, these resonances will be excited when the model is located off central position of the tank.

In the present paper, the effect of the side walls in a lifeboat model tests in a wave flume was investigated numerically and experimentally. A boundary element method based on the Rankine Green function was developed where an artificial damping was introduced in the free surface boundary condition to account for the viscous effect. Sources were also distributed on the side walls, hull surface and far field control surface. Three separation gaps between the side of the model and the flume side wall were investigated. The predicted wave forces, free surface elevations around the model and model motions were compared with the experimental measurements, and good agreement was found.

Due to the existence of the resonance frequencies of the flume width and the non-consideration of viscosity in the potential flow model, numerical results consistently over-predict loads and responses in waves comparing that with the model test measurements. The numerical results with an artificial damping ($\nu = 0.01$–0.025) applied to the free surface boundary condition agree well with the experimental measurements, in particular in the case with the model at an off-central location in the flume. When the model is at the central position of the flume, resonances of some responses (wave elevation, forces and motions of the hull are not excited, the wave field is symmetric about the central plane, variations of wave, loads and motions are smooth. With the model located at an off-central position, the resonances for wave surface elevations, forces and motions are excited, and the viscous effect becomes evident.

It should be mentioned that although viscous damping was introduced in the free surface boundary condition, the governing equation in the model remains that of an ideal (inviscid) fluid, due to the lack of viscous damping, the transverse motions (sway and roll) are still over-predicted.

The present numerical method may also be applied for the assessment of the side wall effect for model experiments in a towing tank or wave tank based on the tank width, water depth and the hull geometries, and to the body-wave interaction problem in a channel.

Acknowledgements

The authors would like to acknowledge the support of the COAST Laboratory of University of Plymouth during the experiments. The funding support from Engineering and Physical Sciences Research Council, United Kingdom through grant EP/N008847/1 is gratefully appreciated.

Appendix A. The Rankine source panel method

Within the potential flow theory, the total velocity potential includes velocity potentials of the incident wave, diffraction wave and radiation waves:

$$\Phi(x,y,z,t) = \Phi_0 + \Phi_7 + \sum_{j=1}^{6} \Phi_j \tag{A-1}$$

where Φ_0 and Φ_7 are velocity potentials of the incident and diffraction waves, respectively, and $\Phi_j, j = 1,\ldots,6$, are velocity potentials of the radiation waves for motions of the 6 degree of freedoms (surge, sway, heave, roll, pitch and yaw, respectively).

The velocity potential of the incident wave:

$$\Phi_0 = Re\{\varphi_0(x,y,z)e^{-i\omega t}\} \tag{A-2}$$

where ω is frequency of the incident wave and the complex spatial incident wave potential is:

$$\varphi_0(x,y,z) = -\frac{iga}{\omega}\frac{\cosh[k_0(z+D)]}{\cosh(k_0D)}e^{ik_0(x\cos\beta+y\sin\beta)} \tag{A-3}$$

where g is acceleration due to gravity, a is amplitude of the incident wave, D is water depth; β is heading angle with $\beta = 180^0$ represents head waves, k_0 is wave number and satisfies the dissipation relation:

$$\omega^2 = gk_0\tanh(k_0D) \tag{A-4}$$

The velocity potential of the diffraction wave

$$\Phi_7 = Re\{\varphi_7(x,y,z)e^{-i\omega t}\} \tag{A-5}$$

Assuming motions of the model are

$$\xi_j = Re\{X_je^{-i\omega t}\} \quad j = 1,2,\ldots,6 \tag{A-6}$$

where X_j is the complex amplitude of model motion. The model velocities are

$$\dot{\xi}_j = Re\{-i\omega X_je^{-i\omega t}\} = Re\{U_je^{-i\omega t}\} \quad j = 1,2,\ldots,6 \tag{A-7}$$

where $U_j = -i\omega X_j$ is the complex velocity amplitude of the j^{th} motion, and the velocity potentials of the radiated waves:

$$\Phi_j(x,y,z,t) = Re\{U_j\varphi_j(x,y,z)e^{-i\omega t}\} \tag{A-8}$$

The velocity potentials φ_j can be solved by the following boundary value problem:

$$\nabla^2\varphi_j = 0 \quad \text{in fluid domain} \tag{A-9}$$

The linearized kinematic free surface condition:

$$\frac{\partial\eta}{\partial t} = \frac{\partial\Phi_j}{\partial z} \text{ on } z = 0 \tag{A-10}$$

and the dynamic free surface condition:

$$\frac{\partial\Phi_j}{\partial t} = -g\eta \text{ on } z = 0 \tag{A-11}$$

From (A-10) and (A-11),

$$\frac{\partial\Phi_j}{\partial z} + \frac{1}{g}\frac{\partial^2\Phi_j}{\partial t^2} = 0 \quad \text{on } z = 0 \tag{A-12}$$

The free surface boundary condition for the spatial velocity potentials is

$$g\frac{\partial\varphi_j}{\partial z} - \omega^2\varphi_j = 0 \quad \text{on } z = 0 \tag{A-13}$$

On the body hull surface:

$$\frac{\partial\varphi_7}{\partial n} = -\frac{\partial\varphi_0}{\partial n} \quad \text{on } S_H \tag{A-14}$$

The body boundary condition for the radiation velocity potentials:

$$\frac{\partial\varphi_j}{\partial n} = n_j \;\; j = 1,2,\ldots,6 \text{ on } S_H \tag{A-15}$$

where $(n_1,n_2,n_3) = \vec{n}$ is the normal vector of the body surface; and $(n_4,n_5,n_6) = \vec{r} \times \vec{n}$. On the bottom:

$$\frac{\partial\varphi_j}{\partial z} = 0 \;\; j = 1,2,\ldots,7 \text{ on } S_B \tag{A-16}$$

On the port and starboard side walls:

$$\frac{\partial\varphi_j}{\partial n} = 0 \;\; j = 1,2,\ldots,7 \text{ on } S_P \text{ and } S_S \tag{A-17}$$

At the far field, the radiation condition is satisfied with (Dai, 1998, Yuan et al., 2018)

$$\frac{\partial\varphi_j}{\partial n} = \frac{\partial\varphi_j}{\partial R} = ik_0\varphi_j \;\; j = 1,2,\ldots,7 \text{ on } S_O \tag{A-18}$$

where $R = \sqrt{(x-\xi)^2 + (y-\eta)^2}$ is the horizontal distance between the source point and the field point. The far field surface, S_O , is part of a vertical cylindrical surface with a large diameter.

In order to prevent the diffracted and radiated waves reaching the free surface boundaries and being reflected back to the body's positions, besides

the radiation condition (A-18), a damping zone was set up on the free surface and it is further away from the body, where the numerical damping term is applied. The numerical damping zone concept was, firstly proposed by Israeli and Orszag (1981), is imposed near the free surface edge. Among several variations of the method that may be observed in the literature, such as the ones applied in Prins (1995), Bunnik (1999), Boo (2002) and Shao (2010), in this work, the formulation applied by Zhen et al. (2010) has been used. A damping factor, μ, is added into the free surface boundary condition (A-10), and (A-11):

$$\frac{\partial \eta}{\partial t} = \frac{\partial \Phi_j}{\partial z} - \mu\eta \text{ on } z = 0 \tag{A-19}$$

and the dynamic free surface condition:

$$\frac{\partial \Phi_j}{\partial t} = -g\,\eta - \mu\,\Phi_j \text{ on } z = 0 \tag{A-20}$$

where $\mu = \nu.\omega$ and ν is the non-dimensional artificial damping coefficient. From (A-19) and (A-20),

$$\frac{\partial \Phi_j}{\partial z} + \frac{1}{g}\frac{\partial^2 \Phi_j}{\partial t^2} + \frac{2\mu}{g}\frac{\partial \Phi_j}{\partial t} + \frac{\mu^2}{g}\Phi_j = 0 \text{ on } z = 0 \tag{A-21}$$

The free surface boundary condition for the spatial velocity potentials is

$$g\frac{\partial \varphi_j}{\partial z} - \left[\omega^2\left(1-\nu^2\right) - i{\cdot}2\nu\omega^2\right]\varphi_j = 0 \text{ on } z = 0 \tag{A-22}$$

One should notice that the undamped free surface elevation is recovered by setting the damping factor ν equal to zero. Various expressions of damping factor have been proposed (Prins, 1995; Bunnik, 1999; Boo, 2002). In this study, ν was set as a constant.

The spatial velocity potentials can be represented by a Rankine source distribution on the domain boundary surfaces:

$$\varphi_j(x,y,z) = \iint_S G(x,y,z;\xi,\eta,\zeta)\cdot\sigma_j(\xi,\eta,\zeta)ds \tag{A-23}$$

where σ_j is the strength of source, $G(x,y,z;\xi,\eta,\zeta)$ is Rankine type Green function and S is the domain boundary.

In the numerical calculations, the boundary surface, S, is discretized into N quadrilateral panels and the source strength on each panel is assumed as constant.

$$\varphi_j(x,y,z) = \sum_{k=1}^{N}\sigma_{jk}\cdot\iint_{\Delta S_k} G(x,y,z;\xi_k,\eta_k,\zeta_k)ds\ (x,y,z) \in S \tag{A-24}$$

$$\nabla\varphi_j(x,y,z) = \sum_{k=1}^{N}\sigma_{jk}\cdot\iint_{\Delta S_k} \nabla G(x,y,z;\xi_k,\eta_k,\zeta_k)ds(x,y,z) \in S \tag{A-25}$$

Substituting (A-24) and (A-25) into the boundary conditions on the body surface, free surface, damping zone, side walls and the outer surface, N equations for the unknown source strength are obtained. After solving the source strength equations, the complex amplitudes of the wave exciting forces and moments are:

$$F_k = i\rho\omega\iint_{S_H}(\varphi_0(\xi,\eta,\zeta) + \varphi_7(\xi,\eta,\zeta))n_k ds\ k = 1,2,\ldots,6 \tag{A-26}$$

Pressure distribution of the radiated waves:

$$p_j(x,y,z,t) = -\rho\frac{\partial \Phi_j}{\partial t} = Re\left\{\rho i\omega U_j\varphi_j e^{-i\omega t}\right\}\ j = 1,2,\ldots,6 \tag{A-27}$$

The complex amplitudes of the k^{th} component of forces/moments on the body hull due to j^{th} mode of body motion are:

$$T_{kj} = Re\left\{i\rho\omega U_j\iint_{S_H}\left(\varphi_j(\xi,\eta,\zeta)\right)n_k ds{\cdot}e^{-i\omega t}\right\}k,j = 1,2,\ldots,6 \tag{A-28}$$

(A-28) is normally expressed as

$$T_{kj} = -A_{kj}\ddot{\xi}_j - B_{kj}\dot{\xi}_j\ k,j = 1,2,\ldots,6 \tag{A-29}$$

where $\ddot{\xi}_j$ and $\dot{\xi}_j$ are acceleration and velocity components of the j^{th} body motions; A_{kj} and B_{kj} are added mass and damping coefficients, respectively. From (A-7), (A-28) can be re-written as

$$T_{kj} = Re\left\{\omega^2 X_j\left[A_{kj} + \frac{i}{\omega}B_{kj}\right]e^{-i\omega t}\right\}\ k,j = 1,2,\ldots,6 \tag{A-30}$$

Substituting (A-6) and (A-7) into (A-29), and comparing (A-29) and (A-30), the added mass and damping coefficients are

$$A_{kj} = Re\left\{\rho\iint_{S_H}\varphi_j n_k ds\right\} \tag{A-31}$$

$$B_{kj} = \omega{\cdot}Im\left\{\rho\iint_{S_H}\varphi_j n_k ds\right\} \tag{A-32}$$

Equations of motion can be written as

$$\sum_{k=1}^{6}\{-\omega^2(M_{kj}+A_{kj})+i\omega B_{kj}+C_{kj}\}X_k=F_j \tag{A-33}$$

where $j=1,2,\ldots,6$, are for surge, sway, heave, roll, pitch and yaw motions, respectively. Solutions of (A-33) and the transfer function of vessel motions.

References

Bertram, V., Thiart, G., 1998. Fully three-dimensional ship seakeeping computations with a surge-corrected Rankine panel method. J. Mar. Sci. Technol. 3 (2), pp94–101.

Boo, Y.Y., 2002. Linear and nonlinear irregular waves and forces in a numerical wave tank. Ocean Eng. 29, 475–493.

Bunnik, T.H.J., 1999. Seakeeping Calculations for Ships, Taking into Account the Non-linear Steady Waves. Technische Universiteit Delft, PhD thesis.

Cao, Y.S., Schultz, W.W., Beck, R.F., 1989. Three-dimensional de-singularized boundary integral equation for three-dimensional non-linear wave problem. In: 4th International Workshop on Water Wave and Floating Bodies, Oystese, Norway.

Chen, J.K., Duan, W.Y., Zhao, B.B., 2018. Hydrodynamics of Side Wall Effects through Image Green Function Based TEBEM, the 33rd International Workshop on Water Waves and Floating Bodies, Brest, France.

Chen, X.B., 1994. On the side wall effects upon bodies of arbitrary geometry in wave tank. Appl. Ocean Res. 16 (6), pp337–345.

Chen, X.B., 2004. Hydrodynamics in offshore and naval applications. In: Proceedings of 6th International Conference on Hydrodynamics, Perth, Australia.

Chen, X.B., Dias, F., 2010. Viscous-potential flow and time harmonic ship waves. In: The 25th International Workshop on Water Waves and Floating Bodies, Harbin, China.

Dai, Y.S., 1998. Potential Flow Theory of Ship Motions in Waves in Frequency and Time Domain. The Defence Industry Press.

Duan, W.Y., Shaheen, H., Chen, X.B., 2007. Tank Side-Wall Effect Evaluated by Using Multi-Body Interaction Computation, 26th International Conference on Offshore Mechanics and Arctic Engineering. San Diego, California, USA.

Faltinsen, O.M., Timokha, A.N., 2015. On damping of two-dimensional piston-mode sloshing in a rectangular moonpool under forced heave motions. J. Fluid Mech. 772. R1-1-R1-11.

Guo, Z.Q., Ma, Q.W., Qin, H.D., 2018. A time-domain Green's function for interaction between water waves and floating bodies with viscous dissipation effects. Water 10 (1), 72.

Guo, Z.Q., Ma, Q.W., Qin, H.D., 2018. A Body-nonlinear Green's function method with viscous dissipation effects for large-amplitude roll of floating bodies. Appl. Sci. 8 (4), 517.

Israeli, M., Orszag, S.A., 1981. Approximation of radiation boundary conditions. J. Comput. Phys. 41, 115–135.

ITTC, 2002. ITTC recommended procedures, testing and extrapolation methods, loads and responses. seakeeping experiments 1, 7.5 - 02- 07-021, Revision 01.

Kashiwagi, M., 1991. Radiation and diffraction forces acting on an offshore structure model in a towing tank. Int. J. Offshore Polar Eng. 1 (2), 101–107.

Kashiwagi, M., Ohkusu, M., 1989. Side-wall effects on hydrodynamic forces acting on a ship with forward and oscillatory motions. In: 5th International Conference on Numerical Ship Hydrodynamics. Hiroshima, Japan, pp. 499–511.

Liapis, S.J., Beck, R.F., 1985. Seakeeping computation using time domain analysis. In: 4th International Conference on Numerical Ship Hydrodynamics, Washington.

Linton, C.M., 1993. On the free-surface Green's function for channel problems. Appl. Ocean Res. 15 (5), pp263–267.

McIver, P., 1993. The wave field scattered by a vertical cylinder in a narrow wave tank. Appl. Ocean Res. 15 (1), 25–37.

Malenica, S., Chen, X.B., 1998. On the irregular frequencies appearing in wave diffraction-radiation solutions. Int. J. Offshore Polar Eng. 8 (2), pp110–114.

Nakos, D.E., 1989. Free surface panel method for unsteady forward speed flow. In: 4th International Workshop on Water Wave and Floating Bodies, Oystese. Norway.

Newman, J.N., 2016. Channel wall effects in radiation-diffraction analysis. In: Proceedings of the 31st International Workshop on Water Waves and Floating Bodies. MI, USA.

Ning, D.Z., Zhu, Y., Zhang, C.W., Zhao, M., 2018. Experimental and numerical study on wave response at the gap between two barges of different draughts. Appl. Ocean Res. 77, pp14–25.

Peng, H., Ali, M.A., Qiu, W., 2015. Hydrodynamic interaction of two bodies in waves. In: 30th International Workshop on Water Waves and Floating Bodies, Bristol, UK.

Pessoa, J., Fonseca, N., Soares, C.G., 2015. Numerical study of the coupled motion responses in waves of side-by-side LNG floating systems. Appl. Ocean Res. 51, pp350–366.

Prins, H., 1995. Time-domain Calculations of Drift Forces and Moments. Technische Universiteit Delft (PhD thesis).

Shao, Y.,L., 2010. Numerical Potential Flow Studies on Weakly Nonlinear Wave-Body Interactions With/without Small Forward Speed, PhD Thesis. Norwegian University of Science and Technology.

Soares, C.G., Taylor, R.E., Ewans, K., 2015. Safe offloading from floating LNG platforms. Appl. Ocean Res. 51, pp252–254.

Sun, L., Taylor, R.E., Taylor, P.H., 2015. Wave driven surface motion in the gap between a tanker and an FLNG barge. Appl. Ocean Res. 51, pp331–349.

Watai, R.A., Dinoi, P., Iglesias, A.S., Simos, A.N., 2015. Rankine time-domain method with application to side-by-side gap flow modelling. Appl. Ocean Res. 50, pp69–90.

Watai, R.A., Ruggeri, F., Simos, A.N., 2016. A new time domain Rankine panel method for simulations involving multiple bodies with large relative displacements. Appl. Ocean Res. 59, pp93–114.

Xia, J.Z., 2001. Evaluation of the Green function for 3-D wave-body interactions in a channel. J. Eng. Math. 40 (1), pp1–16.

Xie, N., Vassalos, D., 2007. Performance analysis of 3D hydrofoil under free surface. Ocean Eng. 34 (8–9), pp1257–1264.

Xie, N., Vassalos, D., 2012. Evaluation of the *m*-terms and 3D ship motion in waves. J. Ship Mech. 16 (9), pp971–979.

Yeung, R.W., 1982. Numerical methods in free surface flows. Annu. Rev. Fluid Mech. 14, pp395–442.

Yuan, Z.M., Zhang, X.S., Ji, C.Y., Jia, L.B., Wang, H.M., Incecik, A., 2018. Side wall effect on ship model testing in a towing tank. Ocean Eng. 147, pp447–457.

Zhao, W.H., Pan, Z.Y., Lin, F., Li, B.B., Taylor, P.H., Efthymiou, M., 2018. Estimation of gap resonance relevant to side-by-side offloading. Ocean Eng. 153, pp1–9.

Zhen, L., Teng, B., Ning, D.Z., Ying, G., 2010. Wave-current interactions with three-dimensional floating bodies. J. Hydrodyn. 22, pp229–240.